Scripta Materialia 199 (2021) 113878

Contents lists available at ScienceDirect

Scripta Materialia

journal homepage: www.elsevier.com/locate/scriptamat

Quantitative mapping of nanotwin variants in the bulk

Jan Schultheiß[a,b,*], Lukas Porz[a], Lalitha Kodumudi Venkataraman[a], Marion Höfling[a], Can Yildirim[c], Phil Cook[c], Carsten Detlefs[c], Semën Gorfman[d], Jürgen Rödel[a], Hugh Simons[e]

[a] Department of Materials and Earth Sciences, Technical University of Darmstadt, 64287 Darmstadt, Germany
[b] Department of Materials Science and Engineering, Norwegian University of Science and Technology, 7034 Trondheim, Norway
[c] European Synchrotron Radiation Facility, 38043 Grenoble, France
[d] Department of Materials Science and Engineering, Tel Aviv University, 69978 Tel Aviv, Israel
[e] Department of Physics, Technical University of Denmark, 2800 Kgs. Lyngby, Denmark

ARTICLE INFO

Article history:
Received 22 January 2021
Revised 5 March 2021
Accepted 11 March 2021
Available online 29 March 2021

Keywords:
Twinning
X-ray diffraction
Domains
Ferroelectricity
Elasto-morphological coupling

ABSTRACT

Crystallographic twins are critical to the properties of numerous materials from magnesium alloys to piezoelectrics. Since the onset of the twin formation is highly sensitive to the triaxial mechanical boundary conditions, non-destructive bulk microscopy techniques are required. Elastic strains can be mapped via X-ray diffraction with a 100-200 nm resolution. However, the interplay of strains with nanotwins cannot be characterized. Here, a method based on dark-field X-ray microscopy to quantify the density of nanotwin variants with twin lamellae of sizes as small as several tens of nanometers in embedded subvolumes (70x200x600 nm^3) in millimeter-sized samples is introduced. The methodology is corroborated by correlating the local density of twin variants to the long-ranging strain fields for a high-performance piezoelectric material. The method facilitates direct, *in situ* mapping and quantification of nanoscale structural changes together with their elastic driving fields, which is the key towards controlling and engineering material's performance at nanometric scales.

Microstructural defects, such as grain or phase boundaries, pores, precipitates, and intermetallic phases are highly effective options for tailoring the performance of twinned materials via engineering the local stress fields [1–3]. A twinned material consists of highly organized alternating twin lamellae of fixed thickness, rigidly connected to each other via a twin boundary [4]. Thermally-induced stress fields around ZnO inclusions can for example increase the operating temperature of relaxor-like piezoelectrics, [5] while strains at twin boundaries can generate localized conducting stripes in iron-based superconductors [6]. Similarly, deformation twinning under applied mechanical stresses is critical to the mechanical properties of various metals, [7,8] inorganic semiconductors, [9] superalloys, [10] or shape-memory alloys [11]. For the most part, the macroscopic performance of these twinned materials is intimately coupled to the local interplay between long-ranging triaxial strain fields and their twin density. [4,12]

The continued development of high-resolution imaging techniques, such as scanning electron or scanning transmission electron microscopy has facilitated the mapping of the twin density from the macroscopic down to the atomic scale at the material's surface. Critically, the formation and activity of twins is sensitive to the local strain state, which varies from triaxial (plane strain) in the bulk to biaxial (plane stress) at the surface [13,14]. Neutron [15,16] and high-energy synchrotron X-ray [17–21] diffraction allow nondestructive strain mapping in the bulk, averaged over a probing volume determined by the beam diameter and penetration depth. Further, a differential-aperture X-ray microscope approach with a sub-micrometer beam diameter enabled visualization of strain fields associated with twin boundaries in polycrystalline magnesium alloys [22]. Similarly, modified Laue-based microscopy enabled to map the onset and time-dependent evolution of such strain fields ~200 µm below the surface [23]. Also, the twinning probability during crack growth in high-entropy alloys was recently quantified using neutron diffraction with millimeter resolution [15]. While scanning a focused X-Ray beam [24–26] further facilitated the mapping of long ranging strain fields with a resolution of 100–200 nm over several micrometers, [27] nanotwins which have lamellae sizes below the spatial resolution of

* Corresponding author.
E-mail address: jan.schultheiss@ntnu.no (J. Schultheiß).

https://doi.org/10.1016/j.scriptamat.2021.113878

the instrument cannot be mapped at this local scale within bulk sampling volumes. This is a critical limitation for materials that must be studied *in situ*, for example, functional components that are part of larger systems or devices.

Here we demonstrate *in situ* mapping of the density of nanotwin variants in the bulk using the rich information in the local reciprocal space maps (RSMs) obtained by dak-field X-ray microscopy [24]. Nanotwin variants are twins with identical orientation of their lamellae. We do this for two grains in the bulk of an industrially promising single-phase ferroelectric/ferroelastic material (rhombohedral crystal structure, *R3m*). Polycrystalline $0.6Ba(Zr_{0.2}Ti_{0.8})O_3$-$0.4(Ba_{0.7}Ca_{0.3})TiO_3$ (BZT-BCT) was prepared using solid-state synthesis by mixing $BaCO_3$ (99.8%), $CaCO_3$ (99.5%), ZrO_2 (99.5%), and TiO_2 (99.6%) in stoichiometric ratio, followed by milling, drying, calcination, and sintering (relative density: 97%, mean grain size: 28.1±5.9 µm). Details on the samples can be found in the supplementary material and in Ref. [28]. BZT-BCT is a perfect model material to demonstrate the strength of our methodology, since the excellent small- and large-signal piezoelectric properties, which exceed 600 pC/N and 1000 pm/V (at 0.5 kV/mm), [29] respectively were related to twin lamellae of 10-100 nm in size [30]. Please note that we adopt a general notation of twin, twin lamella, and twin boundary in this work. Specific to ferroelectrics, these terms correspond to domain, domain size, and domain walls, respectively.

RSMs obtained from micrometer volumes are unsuitable to map and quantify the density of nanotwin variants inside the bulk, since the overlapping diffraction signals from the individual twins form a single peak that may be interpreted as evidence of an untwinned structure (Fig. 1a). We overcome this limitation by obtaining local RSMs from nanoscale subvolumes. Diffraction analysis was performed at beamline ID06 at the European Synchrotron Radiation Facility using X-rays with a photon energy of 17.03 keV (λ =0.728 Å). Both grains were oriented with the 111-scattering vector approximately perpendicular (within 5°) to the electric field *E* (Fig. S1). The optics of the instrument allow a resolution of 70x200x600 nm^3 (local diffraction subvolume $V = 8.4 \cdot 10^6$ nm^3) for local RSMs and strain maps. The 3D subvolume is defined by the spatial resolution of the microscope (70x200 nm^2) and the height of the incident X-Ray beam (600 nm; full width at half maximum (FWHM)). Both image resolution and beam height are physically limited by the numerical aperture of the X-ray lenses and the aberrations present therein. A detailed description of dark-field X-ray microscopy can be found in Refs. [24,31]. In the following, we explain how to utilize the information in the local RSMs to map the density of nanotwin variants and estimate their corresponding size.

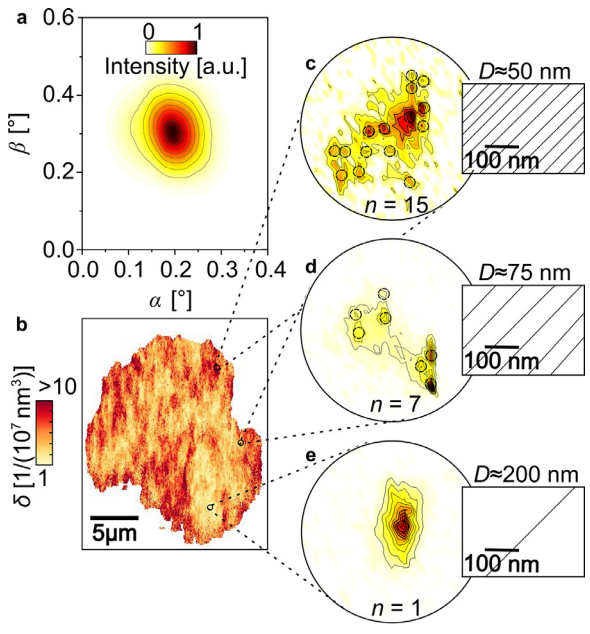

Fig. 1. Methodology to map density of twin variants and their estimated sizes in the bulk of a nano-twinned piezoceramic material. The spatially averaged RSM over all subvolumes (approximately 57 000) of the cross section of a grain is outlined in (a). The density of twin variants, δ, is spatially resolved for the cross section of the grain of the model BZT-BCT material in the virgin state in (b). The density of twin variants was obtained by systematically monitoring RSMs from grain subvolumes (V=70x200x600 nm^3, Fig. S1), while exemplary RSMs obtained from representative subvolumes are depicted in (c)–(e). The splitting of the diffraction peak in the local RSMs (individual peaks are indicated by dashed circles in (c)–(e)) originates from individual twin variants [40] and enables calculation of their density. Subvolumes with a high density of twin variants (δ ~ 10/(10^7 nm^3)) are displayed in red in (b), while subvolumes with a low density of twin variants (δ ~ 1/(10^7 nm^3)) are highlighted in yellow.

Therefore, we obtain local RSMs from ~57 000 nanoscale subvolumes by simultaneously rocking the sample through two perpendicular angles (α, β), non-colinear with the scattering vector (Fig. S1) [24]. This enables to map the density of twin variants across the cross sections of the two grains. Fig. 1b displays the density of twin variants in such a cross section, while the edges of the recorded map are in the vicinity of a grain boundary separating the investigated grain from the surrounding polycrystalline matrix. Exemplified RSMs with a high (small, D ~ 50 nm), medium (medium, D ~ 75 nm), and low (large, D ~ 200 nm) density of twin variants, δ, (estimated size of the twin variants, D) are displayed in Fig. 1c–e, respectively. Individual diffraction peaks in the local RSMs are identified as dashed circles in Fig. 1c–e. In the investigated material, splitting of the peaks in the RSMs may originate from mechanical compatibility of the twins [32] and/or multiple twinning [33]. Please note that other sources of mechanical strain, i.e. dislocations, point defects or twin walls (non-180° domain walls) can be excluded as the main origin for the observed splitting in the local RSMs. Oxides naturally contain a small dislocation density [34,35] and no dislocations were found in undeformed $BaTiO_3$ [36] and polycrystalline $PbTiO_3$ [37]. The strain fields in the vicinity of the twin walls on the other hand can be long ranging (up to 5 µm [27]). A gradual change of the strain, however, most likely results in diffuse scattering [38,39], rather than clear peak splitting in local RSMs.

After having excluded strain fields related to domain walls and dislocations as the main reason for the peak splitting in our local RSMs, we correlate the number of peaks, n, in the local RSMs to individual twin variants [40]. This affords quantification of the density of twin variants (see supplementary material), as

$$\delta = n/V. \quad (1)$$

Note that the local twin density (size of the lamellae) is much higher (smaller) than the values calculated by Eq. (1). One reason is, that twin variants which form a low-intensity peak in the RSM may not be distinguishable from the noise level. Also, twins that diffract at similar α, β values due to a nearly periodic arrangement [30,34] of twins with similarly oriented lamellae cannot be distinguished.

To corroborate our proposed methodology, we next quantify the impact of long-ranging residual elastic stresses and other sources of elastic energy on the density of twin variants in BZT-BCT. We do this by calculating elastic stresses (σ_{111}^{ela}) and related elastic strain energies (U_{111}^{ela}) from the maps of the total strain in <111> direction (ε_{111}^{tot}) [24]. We therefore subtract the strain contributions related to reversible effect, i.e. the electric-field induced piezoelectric effect and domain switching (see supplementary material and Fig. S2), which do not contribute to the elastic stress [41]. The analysis is carried out for a range of electric fields from 0 to 2.5 kV/mm, span-

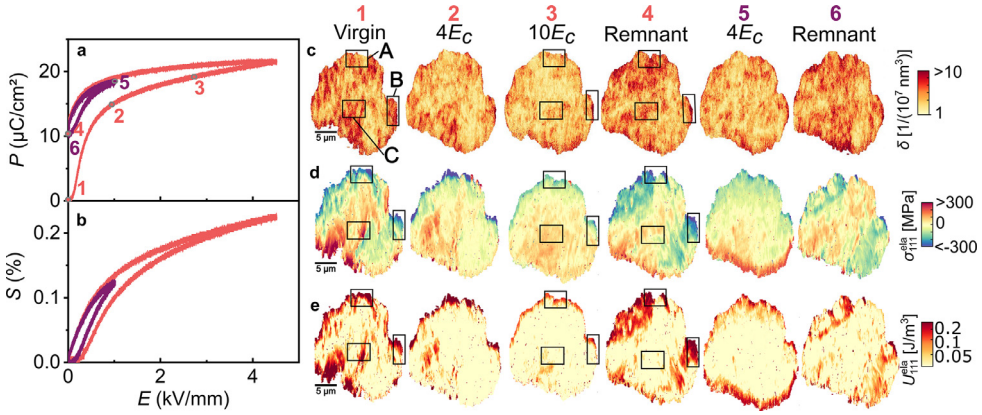

Fig. 2. Electric-field dependent mapping and quantification of the density of twin variants together with their elastic driving fields. Macroscopic unipolar (a) polarization, *P*, and (b) strain, *S*, loops are displayed for the piezoelectric BZT-BCT material in the virgin state. Different electric fields (related to the coercive field, E_c=0.25 kV/mm [42]) are marked by numbers 1–6. A cross section of the grain mapped via dark-field X-ray microscopy under different electric fields is displayed in (c)–(e). We use the methodology introduced in Fig. 1 to calculate the density of twin variants (c), enabling quantification of bulk elasto-morphological correlations as a function of the electric field. Therefore, the local elastic stress, σ_{111}^{ela}, and elastic energy, U_{111}^{ela}, from concurrent strain maps are obtained by subtracting contributions due to the piezoelectric effect and switching strain (Fig. S2 and supplementary material). [41] The calculated elastic parameters σ_{111}^{ela} and U_{111}^{ela} are mapped in (d) and (e), respectively. A local interplay between the density of twin variants and elastic properties is found for the model BZT-BCT material, as demonstrated for subvolumes marked by the letters A-C and discussed in the text. A movie of the electric field-dependent strain evolution is available (supplementary movie 1).

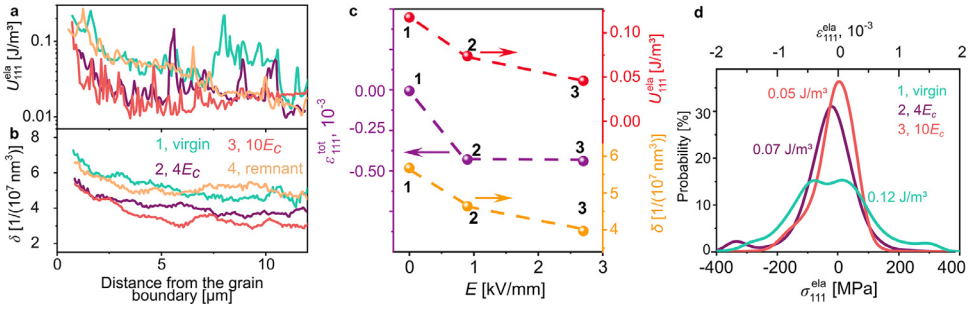

Fig. 3. Quantification of the interplay between elastic driving forces and the density of twin variants. The (a) elastic energy, U_{111}, and (b) density of twin variants, δ, are displayed as a function of the distance from the grain boundary (plotted from the edges of the cross-sectional maps in Fig. 2c). The crystallographically misaligned grains with anisotropic thermal expansion coefficients [44] and spontaneous ferroelastic strain [45] result in an enhancement of the elastic energy and density of twin variants in 4–5 μm vicinity of the grain boundary for all electric fields. The mean value of the elastic energy, U_{111}, total strain, ε_{111}^{tot}, and density of twin variants, δ, decreases with increasing the applied electric field, as displayed in (c). At the same time, electric-field-dependent elastic stress and strain distributions narrow with electric field application, as outlined in (d).

ning and exceeding the coercive electric field (E_c=0.25 kV/mm) where the twins will irreversibly reorient (Fig. 2a and b) [42]. The electric fields were chosen to ensure saturated switching at the highest electric field magnitude (~$10E_c$). Please note that ε_{111}^{tot} for all electric fields is calculated with respect to the averaged unit cell dimension of the virgin state, since a stress-free single crystalline material is not available [43]. The ensuing electric-field dependent density of twin variants, elastic stress, and elastic strain energy is displayed in Fig. 2c–e. A similar analysis for a second grain (grain diameter: 24.5 μm) can be found in supplementary Fig. S3.

The quantitative mapping of the electric field-dependent elasto-morphological correlations now allows us to correlate the density of twin variants to local electric-field dependent elastic driving forces. First, we provide the density of twin variants together with the long-ranging elastic strain fields as a function of distance from the grain boundary (outer edges of the cross sections of the grain in Fig. 2c–e) to the grain interior (Fig. 3a and b). Contrary to expectations, [27] we find that the elastic stresses in the vicinity of the grain boundary can be as high as ±300 MPa and are generally higher in the virgin state than during or after poling. This is indicated by a 60% decrease of the local U_{111}^{ela} in the periphery compared to the center of the grain (Fig. 3a). The quantified spatial inhomogeneities of the strain energy originate from an anisotropic thermal expansion coefficient, the random orientation of individual crystallites, [44] and the spontaneous strain formed at the phase transition in ferroelastic materials [45,46]. Stress concentrations in the periphery of the grain boundary might be related to the complexity of the polycrystalline microstructure, i.e. triple-grain junctions, or glass phases at the grain boundary. Please note that in comparison to previous works quantifying the elastic energy along a grain boundary, [44,47] experimental data in Fig. 3a is measured under triaxial mechanical boundary conditions in the bulk.

Since the stresses we observed locally exceed the coercive stress of BZT-BCT (obtained during macroscopic compression tests, $\sigma_c \sim -25$ MPa [48]), significant switching is expected in the vicinity of the grain boundary (Fig. 3b). Using our approach, we find that the decrease of the elastic energy as a function of the distance from the grain boundary corresponds to a decrease of the average density of twin variants. This demonstrates the possibility of a locally engineered density of twin variants via mechanical stresses. In particular, the density of twin variants ($\delta \sim 4.8/(10^7\ nm^3)$) found for subvolumes inside the grain (>4–5 μm from the grain boundary) was typically 30% smaller compared to subvolumes in the vicinity of the grain boundary ($\delta \sim 6.2/(10^7\ nm^3)$).

The *in situ* quantification of the density of twin variants and activating elastic driving forces under applied electric fields enables investigation of the effect of the electric field on the elasto-morphological correlations (Fig. 3c and d). The high density of

twin variants and the inhomogeneous elastic stresses in the virgin state are likely related to the complex phase equilibria of the investigated system [29]. Increasing the electric field up to 2.7 kV/mm (~$10E_c$) decreases the average density of twin variants by approximately 35% compared to the virgin state (Fig. 3c, $\delta^{(10E_c)} = 3.8/(10^7\text{nm}^3)$, $\delta^{\text{virgin}} = 5.8/(10^7\text{nm}^3)$). Notably, this decrease in the density of twin variants corresponds to a 40% decrease in the macroscopic piezoelectric d_{33} coefficient at the same electric field magnitude, [49] corroborating the impact of nanotwins on the electromechanical functionality. At the same time, the U_{111}^{ela} is reduced by 60% for an electric field of 2.7 kV/mm (~$10E_c$) in comparison to the virgin state, corresponding to a narrowing of the distribution of the elastic stresses with electric field application. As highlighted in Fig. 3d, the FWHM of the stress distribution decreases by 40% and 50% for applied electric fields of 0.9 kV/mm (~$4E_c$) and 2.7 kV/mm (~$10E_c$) relative to the virgin state, respectively.

While the averaged electric-field response corroborates with the macroscopic functional performance of the material, we also show that the local response is very inhomogeneous. Examples are highlighted for the subvolumes in A-C in Fig. 2c–e. For the subvolumes in A, the density of twin variants and elastic stress reduce when an electric field of $10E_c$ is applied, while subvolumes in B remain largely unchanged, indicating the effect of local pinning centers on ferroelectric/ferroleastic domain wall movement [50,51] For the subvolumes in C, the density of twin variants and elastic energy are substantially diminished and a monodomain-like state in the center of the grain can be identified [30]. With this, our methodology enables mapping of the electric-field induced changes of the density of twin variants highly spatially resolved [19]. In addition, it quantifies the interplay between local electric field-induced switching and elastic stresses, indicating electric-field induced stress-releasing effects in the bulk, mimicking microstructural texturing approaches [52,53].

In conclusion, we present a methodology for visualizing and quantifying the density and corresponding sizes of twin variants within nanometric volumes in the bulk. Moreover, we compare these morphological characteristics directly to maps of the local elastic stresses and energies. In demonstrating the method, we outline the localized tunability of the density of twin variants via mechanical stresses induced by intergranular coupling for a modern, lead-free ferroelectric/ferroelastic material. Specifically, we highlight that the electric field narrows the distribution of elastic stresses and reduces elastic energies by 60%, while simultaneously decreasing the density of twin variants by 35%, giving the grain a single-crystalline like character. Further, we underline electric-field effects on the macroscopic piezoelectric performance. Broadly speaking, this confirms the potential and relevance of the methodology for all twinned materials, where the plane strain state in the bulk together with mapping of the density of twin variants provides insight far beyond highly localized surface techniques or conventional diffraction-based imaging.

The comprehensive multi-length scale mapping of nanostructures and stresses is a key step towards controlling local elasto-morphological correlations and thus the performance of many twinned materials. Combining the methodology with 3D tomography approaches [54,55] further enables to optimize the elasto-morphogical correlations beyond the investigated cross section of the grain. This is important for emerging fields in complex oxides, such as high-permittivity applications, phase transitions or domain wall dynamics, which exhibit a complex local coupling between elastic energies and nanoscale twin variants. The approach we present here can be applied to all twin systems, e.g. martensitic materials, superalloys, or high entropy systems, where the interplay between elastic strain und nanotwins under external stimulation is crucial towards realizing high performance. *In situ* measurements of the evolution of strain and density of twin variants further enables the discussion of elasto-plastic boundary conditions on twinning, using theoretical models [56,57].

Declaration of Competing Interest

None

Acknowledgment

We are grateful to the European Synchrotron Radiation Facility for providing beamtime at ID06. J.S. and L.K.V. acknowledge the support of the Alexander von Humboldt Foundation through the Feodor-Lynen fellowship and the Alexander von Humboldt fellowship. M.H., L.P., and J.R. thank the Deutsche Forschungsgemeinschaft (DFG) for support under project number 414179371. H.S. acknowledges support from ERC Starting Grant #804665. C.Y. acknowledges Onderzoeks Centrum voor de Aanwending von Staal (OCAS) for financial support. H.F. Poulsen is acknowledged for helpful discussions and careful proof reading. V. Rojas is acknowledged for preparing the samples, D. Meier for helpful instructions.

Supplementary materials

Supplementary material associated with this article can be found, in the online version, at doi:10.1016/j.scriptamat.2021.113878.

References

[1] D. Raabe, S. Sandlobes, J. Millan, D. Ponge, H. Assadi, M. Herbig, P.P. Choi, Acta Mater. 61 (16) (2013) 6132–6152.
[2] M.U. Rothmann, W. Li, Y. Zhu, U. Bach, L. Spiccia, J. Etheridge, Y.-B. Cheng, Nat. Commun. 8 (1) (2017) 1–8.
[3] G. Arlt, J. Mater. Sci. 25 (6) (1990) 2655–2666.
[4] R.W. Cahn, Adv. Phys. 3 (12) (1954) 363–445.
[5] L.M. Riemer, K.V. Lalitha, X.J. Jiang, N. Liu, C. Dietz, R.W. Stark, P.B. Groszewicz, G. Buntkowsky, J. Chen, S.T. Zhang, J. Rödel, J. Koruza, Acta Mater. 136 (2017) 271–280.
[6] A. Yagil, Y. Lamhot, A. Almoalem, S. Kasahara, T. Watashige, T. Shibauchi, Y. Matsuda, O.M. Auslaender, Phys. Rev. B 94 (6) (2016) 064510.
[7] W. Wu, Y. Gao, N. Li, C.M. Parish, W. Liu, P.K. Liaw, K. An, Acta Mater. 121 (2016) 15–23.
[8] L.Y. Wang, Z.H. Huang, H.M. Wang, A. Maldar, S.B. Yi, J.S. Park, P. Kenesei, E. Lilleodden, X.Q. Zeng, Acta Mater. 155 (2018) 138–152.
[9] Y. Oshima, A. Nakamura, K. Matsunaga, Science 360 (6390) (2018) 772–774.
[10] D. Naujoks, Y.M. Eggeler, P. Hallensleben, J. Frenzel, S.G. Fries, M. Palumbo, J. Kossmann, T. Hammerschmidt, J. Pfetzing-Micklich, G. Eggeler, E. Spiecker, R. Drautz, A. Ludwig, Acta Mater. 138 (2017) 100–110.
[11] T. Birk, S. Biswas, J. Frenzel, G. Eggeler, Shape Mem. Superelast. 2 (2) (2016) 145–159.
[12] E.K.H. Salje, Annu. Rev. Mater. Res. 42 (2012) 265–283.
[13] S. Kong, N. Kumar, S. Checchia, C. Cazorla, J. Daniels, Adv. Funct. Mater. 29 (27) (2019) 1900344.
[14] J.-Q. Yan, J.-S. Zhou, J. Goodenough, Phys. Rev. B 70 (1) (2004) 014402.
[15] T.-N. Lam, S.Y. Lee, N.-T. Tsou, H.-S. Chou, B.-H. Lai, Y.-J. Chang, R. Feng, T. Kawasaki, S. Harjo, P.K. Liaw, Acta Mater. 201 (2020) 412–424.
[16] Q. Xie, Y. Chen, P. Yang, Z. Zhao, Y.D. Wang, K. An, Scr. Mater. 150 (2018) 168–172.
[17] B.C. Larson, W. Yang, G.E. Ice, J.D. Budai, J.Z. Tischler, Nature 415 (6874) (2002) 887–890.
[18] Y. Hayashi, D. Setoyama, Y. Hirose, T. Yoshida, H. Kimura, Science 366 (6472) (2019) 1492–1496.
[19] A. Pramanick, D. Damjanovic, J.E. Daniels, J.C. Nino, J.L. Jones, J. Am. Ceram. Soc. 94 (2) (2011) 293–309.
[20] Y. Wang, E.-W. Huang, Y. Ren, Z. Nie, G. Wang, Y. Liu, J. Deng, H. Choo, P. Liaw, D. Brown, Acta Mater. 56 (4) (2008) 913–923.
[21] J. Schultheiß, L. Liu, H. Kungl, M. Weber, L. Kodumudi Venkataraman, S. Checchia, D. Damjanovic, J.E. Daniels, J. Koruza, Acta Mater. 157 (2018) 355–363.
[22] L. Balogh, S.R. Niezgoda, A.K. Kanjarla, D.W. Brown, B. Clausen, W. Liu, C.N. Tome, Acta Mater. 61 (10) (2013) 3612–3620.
[23] P.A. Lynch, M. Kunz, N. Tamura, M.R. Barnett, Acta Mater. 78 (2014) 203–212.
[24] M. Kutsal, P. Bernard, G. Berruyer, P.K. Cook, R. Hino, A.C. Jakobsen, W. Ludwig, J. Ormstrup, T. Roth, H. Simons, K. Smets, J.X. Sierra, J. Wade, P. Wattecamps, C. Yildirim, H.F. Poulsen, C. Detlefs, IOP Conf. Ser. 580 (2019) 012007.
[25] R.C. Rogan, N. Tamura, G.A. Swift, E. Üstündag, Nat. Mater. 2 (6) (2003) 379–381.

[26] T.T. Lummen, Y. Gu, J. Wang, S. Lei, F. Xue, A. Kumar, A.T. Barnes, E. Barnes, S. Denev, A. Belianinov, Nat. Commun. 5 (1) (2014) 1–9.
[27] H. Simons, A.B. Haugen, A.C. Jakobsen, S. Schmidt, F. Stöhr, M. Majkut, C. Detlefs, J.E. Daniels, D. Damjanovic, H.F. Poulsen, Nat. Mater. 17 (9) (2018) 814–819.
[28] V. Rojas, J. Koruza, E.A. Patterson, M. Acosta, X.J. Jiang, N. Liu, C. Dietz, J. Rödel, J. Am. Ceram. Soc. 100 (10) (2017) 4699–4709.
[29] J.H. Gao, D.Z. Xue, W.F. Liu, C. Zhou, X.B. Ren, Actuators 6 (3) (2017) 24.
[30] H. Guo, C. Zhou, X. Ren, X. Tan, Phys. Rev. B 89 (10) (2014) 100104(R).
[31] H.F. Poulsen, P.K. Cook, H. Leemreize, A.F. Pedersen, C. Yildirim, M. Kutsal, A.C. Jakobsen, J.X. Trujillo, J. Ormstrup, C. Detlefs, J. Appl. Crystallogr. 51 (2018) 1428–1436.
[32] N.T. Tsou, J.E. Huber, Mech. Mater. 42 (7) (2010) 740–753.
[33] G. Gottstein, Acta Metall. 32 (7) (1984) 1117–1138.
[34] C.A. Randall, D.J. Barber, R.W. Whatmore, J. Mater. Sci. 22 (3) (1987) 925–931.
[35] O. Eibl, P. Pongratz, P. Skalicky, H. Schmelz, Phys. Status Solidi A 108 (2) (1988) 495–502.
[36] P. Ren, M. Höfling, J. Koruza, S. Lauterbach, X. Jiang, T. Frömling, D.K. Khatua, C. Dietz, L. Porz, R. Ranjan, J. Am. Ceram. Soc. 103 (3) (2020) 1891–1902.
[37] I. MacLaren, L.A. Schmitt, H. Fuess, H. Kungl, M.J. Hoffmann, J. Appl. Phys. 97 (9) (2005) 094102.
[38] J.E. Daniels, J.L. Jones, T.R. Finlayson, J. Phys. D Appl. Phys. 39 (24) (2006) 5294–5299.
[39] N. Floquet, C.M. Valot, M.T. Mesnier, J.C. Niepce, L. Normand, A. Thorel, R. Kilaas, J. Phys. III 7 (6) (1997) 1105–1128.
[40] B. Jakobsen, H.F. Poulsen, U. Lienert, J. Almer, S.D. Shastri, H.O. Sørensen, C. Gundlach, W. Pantleon, Science 312 (5775) (2006) 889–892.
[41] D.A. Hall, A. Steuwer, B. Cherdhirunkorn, T. Mori, P.J. Withers, Acta Mater. 54 (11) (2006) 3075–3083.
[42] M. Zakhozheva, L.A. Schmitt, M. Acosta, H. Guo, W. Jo, R. Schierholz, H.J. Kleebe, X. Tan, Phys. Rev. Appl. 3 (6) (2015) 064018.
[43] P. Veber, F. Benabdallah, H.R. Liu, G. Buse, M. Josse, M. Maglione, Materials 8 (11) (2015) 7962–7978.
[44] V.R. Vedula, S.J. Glass, D.M. Saylor, G.S. Rohrer, W.C. Carter, S.A. Langer, E.R. Fuller, J. Am. Ceram. Soc. 84 (12) (2001) 2947–2954.
[45] W.R. Buessem, L.E. Cross, A.K. Goswami, J. Am. Ceram. Soc. 49 (1) (1966) 33–36.
[46] K. Aizu, Phys. Rev. B 2 (3) (1970) 754.
[47] A. Zimmermann, E.R. Fuller, J. Rödel, J. Am. Ceram. Soc. 82 (11) (1999) 3155–3160.
[48] M.C. Ehmke, F.H. Schader, K.G. Webber, J. Rödel, J.E. Blendell, K.J. Bowman, Acta Mater. 78 (2014) 37–45.
[49] M. Acosta, N. Novak, G.A. Rossetti, J. Rödel, Appl. Phys. Lett. 107 (14) (2015) 142906.
[50] D.M. Marincel, H.R. Zhang, A. Kumar, S. Jesse, S.V. Kalinin, W.M. Rainforth, I.M. Reaney, C.A. Randall, S. Trolier-McKinstry, Adv. Funct. Mater. 24 (10) (2014) 1409–1417.
[51] J. Schultheiß, S. Checchia, H. Uršič, T. Frömling, J. Daniels, B. Malič, T. Rojac, J. Koruza, J. Eur. Ceram. Soc. 40 (12) (2020) 3965–3973.
[52] C. Ming, T.N. Yang, K. Luan, L. Chen, L. Wang, J.T. Zeng, Y.X. Li, W.Q. Zhang, L.Q. Chen, Acta Mater. 145 (2018) 62–70.
[53] J. Schultheiß, O. Clemens, S. Zhukov, H. Seggern, W. Sakamoto, J. Koruza, J. Am. Ceram. Soc. 100 (5) (2017) 2098–2107.
[54] M.P. Echlin, A. Mottura, C.J. Torbet, T.M. Pollock, Rev. Sci. Instrum. 83 (2) (2012) 023701.
[55] A.B. Mosberg, E.D. Roede, D.M. Evans, T.S. Holstad, E. Bourret, Z. Yan, A.T.J. van Helvoort, D. Meier, Appl. Phys. Lett. 115 (12) (2019) 122901.
[56] B. Clausen, C. Tomé, D. Brown, S. Agnew, Acta Mater. 56 (11) (2008) 2456–2468.
[57] Z.Y. Zhang, R.D. James, S. Muller, Acta Mater. 57 (15) (2009) 4332–4352.